Monthly Notices of the ROYAL ASTRONOMICAL SOCIETY

MNRAS **516,** 3778–3785 (2022) https://doi.org/10.1093/mnras/stac2349
Advance Access publication 2022 August 29

High mass flow rate in a BAL outflow of quasar SDSS J1130 + 0411

Andrew Walker ,★ Nahum Arav and Doyee Byun
Department of Physics, Virginia Tech, Blacksburg, VA 24061, USA

Accepted 2022 August 17. Received 2022 August 15; in original form 2022 May 12

ABSTRACT

We present the analysis of the absorption troughs of six outflows observed in quasar SDSS J1130 + 0411 ($z \approx 3.98$) with radial velocities ranging from −2400 to −15 400 km s^{-1}. These spectra were taken with the Very Large Telescope/Ultraviolet and Visual Echelle Spectrograph over the rest-frame wavelength range of 1135–1890 Å. In the main outflow system ($v \approx -3200$ km s^{-1}), we identify Fe II and several Fe II* absorption troughs, as well as Si II and Si II* troughs, which we use to determine the electron number density $\log n_e = 2.6^{+0.8}_{-0.7}$ cm^{-3}. Using the column densities of these and other ions, we determine a photoionization solution with hydrogen column density $\log N_H = 21.44^{+0.24}_{-0.33}$ cm^{-2} and ionization parameter $\log U_H = -1.75^{+0.28}_{-0.45}$. From these values, we derive the distance $R = 16^{+23}_{-11}$ kpc, the average mass flow rate $\dot{M} = 4100^{+6600}_{-2400}$ M$_\odot$ yr^{-1}, and the kinetic luminosity $\log \dot{E}_k = 46.13^{+0.41}_{-0.37}$ erg s^{-1}. This $\dot{E}_k$ is $1.4^{+2.2}_{-0.8}$ per cent of the quasar's Eddington luminosity, and therefore contributes significantly to AGN feedback.

Key words: galaxies: evolution – galaxies: kinematics and dynamics – quasars: absorption lines – quasars: emission lines – quasars: general – quasars: individual: SDSS J113010.58 + 041128.0.

1 INTRODUCTION

Quasar outflows can be identified by absorption troughs that are blueshifted relative to the rest frame of active galactic nuclei (AGNs; e.g. Hewett & Foltz 2003; Dai, Shankar & Sivakoff 2008; Knigge et al. 2008). Three main types of AGN absorption lines have been defined: broad absorption lines (BALs), narrow absorption lines (NALs), and mini-BALs. BALs are defined by continuous absorption below 90 per cent residual intensity with a velocity width $\Delta v \gtrsim 2000$ km s^{-1} and are found in ∼20 per cent of quasar spectra (Hamann & Sabra 2003; Stone & Richards 2019). NALs have continuous absorption less than a few hundred km s^{-1} wide, and are found in ∼60 per cent of spectra (Hamann & Sabra 2003; Miller et al. 2018; Stone & Richards 2019). Mini-BALs are an intermediate category, with velocity widths $500 \lesssim \Delta v \lesssim 2000$ km s^{-1} and a detection rate of ∼5 per cent (Hamann & Sabra 2003; Hidalgo et al. 2012; Arav et al. 2020).

Quasar outflows can have a number of effects on the AGN environment, including contributing to the chemical evolution of their host galaxies by ejecting large quantities of metal and energy (e.g. Matteo, Springel & Hernquist 2005; Moll et al. 2006) and affecting star formation outside of the AGN by releasing angular momentum from accretion winds (e.g. Murray et al. 1995; Proga, Stone & Kallman 2000). Quasar outflows are also believed to have the potential to contribute to AGN feedback (e.g. Ciotti, Ostriker & Proga 2009; Hopkins & Elvis 2009; McCarthy et al. 2010; Anglés-Alcázar et al. 2016; Vayner et al. 2021). Theoretical models suggest that for an outflow to effectively contribute to this feedback, its kinetic luminosity $\dot{E}_k$ must be at least 0.5 per cent − 5 per cent of the Eddington luminosity ($L_{\rm Edd}$) of the quasar's supermassive black hole (Hopkins & Elvis 2009; Scannapieco & Oh 2004, respectively). Observations show that these criteria can be met (e.g. Moe et al. 2009; Arav et al. 2013, 2020; Chamberlain, Arav & Benn 2015; Xu et al. 2019, 2020a, b; Choi et al. 2020, 2022; Miller et al. 2020a, b; Byun, Arav & Walker 2022a; Byun, Arav & Hall 2022b). The distance between the central source and the outflow (R) and the total hydrogen column density (N_H) are crucial in determining $\dot{E}_k$, and thus whether the outflow could have a significant role in AGN feedback. We can determine R by finding the ionization parameter (U_H) and the electron number density (n_e), as many studies in the past have done (e.g. de Kool et al. 2001, 2002; Hamann et al. 2001; Gabel et al. 2005; Borguet et al. 2012; Xu et al. 2018; Arav et al. 2020; Miller et al. 2020a; Choi et al. 2022; Byun et al. 2022a, b). The column densities of various ions in a system can be used to find N_H and U_H, and n_e can be found from the ratios of excited state to ground state ionic column densities (Arav et al. 2018). In this paper, we make a determination of R, N_H, and $\dot{E}_k$ for an outflow found in the Very Large Telescope/Ultraviolet and Visual Echelle Spectrograph (VLT/UVES) spectrum of SDSS J113010.58 + 041128.0 (hereafter J1130 + 0411).

We obtained the data for this object from the Spectral Quasar Absorption Database (SQUAD) data release 1 (Murphy et al. 2018), a survey of 475 quasars whose spectral data were collected from VLT/UVES. While searching through this data base, we found that J1130 + 0411 possessed prominent absorption, including excited state lines, which suggested an outflow. We derive a systemic redshift $z = 3.98$ (see Section 2.1), and we identify the outflow velocity $v = -3200$ km s^{-1} system to be BAL system, as the C IV trough has $\Delta v \sim 2200$ km s^{-1}. Here, we focus on this system as within it we observe excited states of Fe II and Si II. These lines are important as they are largely unblended in the spectrum, and so we can use them in order to determine n_e, and thus R. Additionally, we find that this BAL system has a particularly

★ E-mail: aiwalker@vt.edu

high average mass flow rate $\dot{M} = 4100^{+6600}_{-2400}$ $M_\odot$ yr^{-1} that is, for example, almost 10 times higher than the largest $\dot{M}$ objects seen in the Choi et al. (2022) FeLoBAL sample and comparable to an outflow system in J0242 + 0049 analysed by Byun et al. (2022a; see Section 5.2).

This paper is organized as follows. In Section 2, we present the details of the observation and data acquisition of J1130 + 0411. Section 3 describes the analysis process including the spectral fitting to measure ionic column densities and the determination of the parameters N_H, U_H, and n_e. In Section 4, we then utilize these values and present our calculations of R, $\dot{M}$, and $\dot{E}_k$. Section 5 discusses our results, compares with other works, and describes the other seven absorption components in J1130 + 0411. Section 6 summarizes this paper. We adopt a cosmology of $h = 0.696$, $\Omega_m = 0.286$, and $\Omega_\Lambda = 0.714$ (Bennett et al. 2014).

2 OBSERVATIONS

The quasar J1130 + 0411 (J2000: RA = 11:30:10, Dec. = + 04:11:28, $z = 3.98$, see Section 2.1) was observed on 2008 February 12 and 14 with VLT/UVES as part of the program 080.B-0445(A), with overall wavelength coverage 3670–9467 Å. The spectral data has a resolution $R \simeq 40\,000$ and a signal-to-noise ratio $S/N \simeq 37$. The data were combined, reduced, and normalized by Murphy et al. (2018) as part of their SQUAD Data Release 1. Fig. 1 displays the full normalized spectrum. We identify eight absorption systems in this quasar, named S1-8 in order of decreasing velocity (see Table 1). The main focus of this paper is on the BAL outflow, S5, while the other systems are covered in Section 5.3.

2.1 Determination of redshift

In order to measure the width of the C IV BAL, measure the width of the C IV emission line (see Section 5.1), and determine the redshift of J1130 + 0411, we retrieved an SDSS spectrum from MJD = 52642 (2003 January 3). Fig. 2 shows this unnormalized spectrum with the main absorption troughs labelled. Note that the vertical lines are not centred in many of the BALs. The high-column density of these ions allows for higher velocities in the outflow, thus widening the blue side of the BAL. Additionally, S4 is blended with the blue side of these BALs.

For J1130 + 0411, we determine a systemic redshift $z = 3.98$ that lines up with the C II/C II* and Si IV emission lines. As an additional check, this redshift places the Ly α line ~6 Å blueward of the edge of the Lyman α forest in the rest frame. This estimate is different from the one made by Chen et al. (2021), who determine a redshift of $z = 3.930$ that appears to instead line up with the BAL outflow. Chen et al. (2021) also identify one C IV absorption system. Using their reported redshift to calculate absorption system velocities, we find that this system best matches our highest velocity system, S1. They did not identify S5, as this C IV absorption falls in the spectral gap of this UVES data (7521–7666 Å observed wavelength).

Our redshift is also different from the redshift reported on the SDSS website, $z = 5.25$. SDSS uses an algorithm in order to determine the redshift of objects in its catalog, and this algorithm does not always produce accurate measurements. It is clear by eye that their reported redshift does not coincide with any emission features in the unnormalized spectrum.

3 DATA ANALYSIS

3.1 Spectral fitting

The first step in determining the physical characteristics of an outflow is to determine the column densities of the ions observed in the system. The simplest way of doing this is to use the apparent optical depth (AOD) method, which assumes that the outflow completely and uniformly covers the source (Savage & Sembach 1991). In this case, the normalized flux is related to the optical depth by

$$I(v) = \exp(-\tau(v)), \tag{1}$$

where I is the observed flux and τ is the optical depth. The column density can found by

$$N_{\rm ion} = \frac{m_e c}{\pi e^2 f \lambda} \int \tau(v) {\rm d}v, \tag{2}$$

where m_e is the electron mass, c is the speed of light, e is the elementary charge, and f and λ are the oscillator strength and wavelength of the transition line, respectively. This method only gives a lower limit to the column density. If an ion presents as a doublet or multiplet, we can use the more accurate partial covering (PC) method (Barlow, Hamann & Sargent 1997; Arav et al. 1999a, b), which accounts for effects such as non-black saturation (Edmonds et al. 2011; Borguet et al. 2012). This method introduces a velocity-dependent covering fraction $C(v)$ (de Kool et al. 2002; Arav et al. 2005), and the normalized flux depends on the optical depth by

$$\begin{aligned} I_1(v) &= [1 - C(v)] + C(v)e^{-\tau(v)}, \\ I_2(v) &= [1 - C(v)] + C(v)e^{-R_{21}\tau(v)}, \end{aligned} \tag{3}$$

where I_1 and I_2 are the normalized fluxes of the doublet transition lines, and $R_{21} = f_2\lambda_2/f_1\lambda_1$. Here, f_1, f_2, λ_1, and λ_2 are the oscillator strengths and wavelengths of the two doublet lines. We adopt column densities calculated using PC rather than AOD whenever possible.

Many of the absorption lines are blended with other troughs, so we model each trough by fitting to an unblended section of the trough a Gaussian of the form

$$\tau_i(v) = \frac{A_i}{\sigma_i\sqrt{2\pi}} * \exp\left(\frac{-(v - v_i)^2}{2\sigma_i^2}\right), \tag{4}$$

$$I_i(v) = \exp(-\tau_i(v)) \tag{5}$$

where, for trough i, A_i is the scaling factor, σ_i is the velocity dispersion (FWHM $= 2\sigma\sqrt{2\ln(2)}$), and v_i is the velocity centroid. For example, in many cases, the blue wing of the trough is the only unblended portion and therefore is what the Gaussian is fitted to. For S5 in particular, we observe both a wide and a narrow component in most lines, so for this system, we use a double Gaussian to fit the troughs, i.e., $I_i = I_{\rm wide} \times I_{\rm narrow}$.

Compared with Si II 1260 and 1304 Å, the Si II 1808 Å trough is shallow and narrow, and so we assume it is unsaturated and interpret its AOD column density as a measurement rather than a lower limit. We observe non-black saturation in the Al III λλ1854, 1860 BAL, so we obtain a measurement for its column density using the PC method. For all other BALs, we use the AOD method to obtain a lower limit. Table 2 gives the column densities we adopted in this analysis. We add 20 per cent error in quadrature to the column density errors in order to account for uncertainty in the continuum model (Xu et al. 2018). Note that the adopted Fe II column density is somewhat higher than that of the AOD value. This is because four of the Fe II* energy levels show more than one trough for the same level, and so for these we use the PC solution. We then add these measurements to the AOD

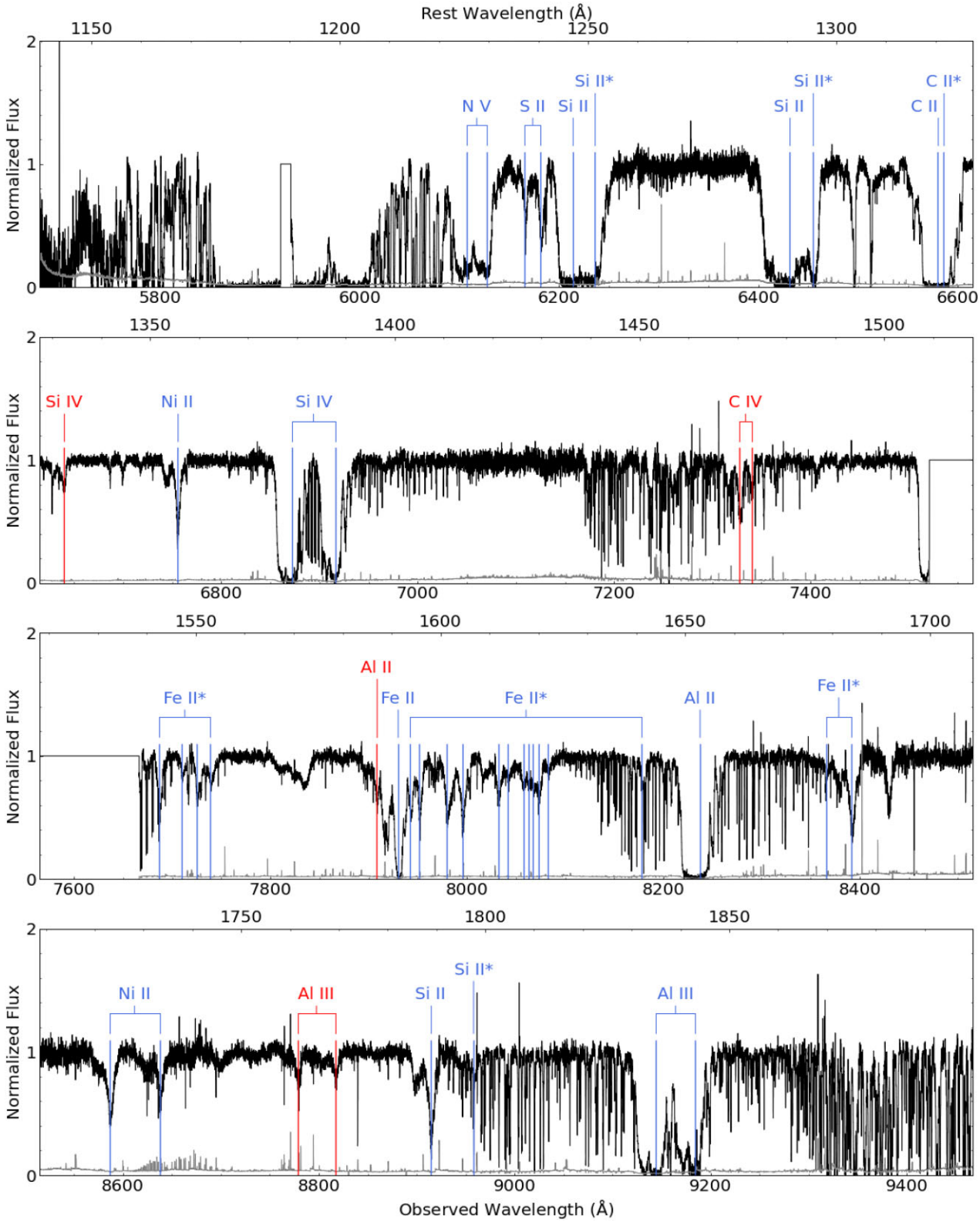

Figure 1. Normalized spectrum of J1130 + 0411 from the 2018 SQUAD data release (Murphy et al. 2018). Troughs of the main system S5 are presented in blue. Troughs of the highest velocity system S1, identified by Chen et al. (2021), are presented in red. Only the red absorption trough of Si IV in S1 is labelled, as the blue trough is blended with the C II troughs of lower velocity systems and we do not obtain a column density from it. Note that one of the Si II/Si II* BALs (1527 and 1533 Å rest wavelength) and the C IV BAL are in a wavelength gap not covered by UVES (7521–7666 Å observed wavelength).

Table 1. Properties of all absorption systems in J1130 + 0411.

System	Velocity (km s^{-1})	log(N_H) (cm^{-2})	log(U_H)	Status
S1	−15 400	...	...	outflow
S2	...[a]	...	...	intervening
S3	...[b]	$21.10^{+0.65}_{-2.80}$	$-1.47^{+0.62}_{-2.37}$	intervening
S4	−3600	$21.79^{+0.01}_{-2.48}$	$-1.18^{+0.03}_{-2.13}$	S5 subcomponent
S5	−3200	$21.44^{+0.24}_{-0.33}$	$-1.75^{+0.28}_{-0.45}$	outflow (main)
S6	−2700	$>19.95_{-1.04}$	$-3.17^{+0.58}_{-0.12}$	outflow
S7	−2600	...	...	outflow
S8	−2400	$>19.97_{-0.13}$	$>-2.99_{-1.03}$	outflow

[a] The redshift of the intervening system S2 is $z = 3.798$.
[b] The redshift of the intervening system S3 is $z = 3.912$.

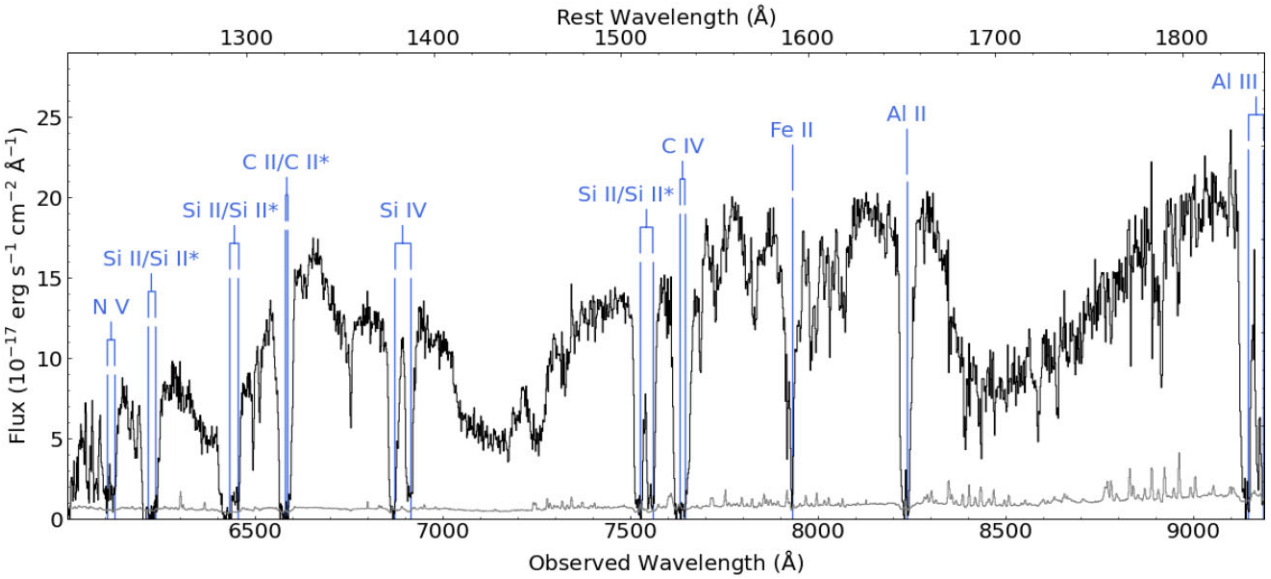

Figure 2. Unnormalized spectrum from SDSS. The locations of prominent BALs are marked in blue.

Table 2. Column densities of ions in main system of J1130 + 0411 (in units of 10^{12} cm^{-2}).

Ion	AOD	PC	Adopted
C II	6700^{+950}_{-26}	...	$>6700_{-1300}$
N V	2900^{+23}_{-21}	...	$>2900_{-580}$
Al II	180^{+25}_{-1}	...	$>180_{-40}$
Al III	780^{+82}_{-15}	860^{+10}_{-140}	860^{+170}_{-220}
Si II	$31\,000^{+1500}_{-1500}$	...	$31\,000^{+6400}_{-6400}$
Si IV	1100^{+13}_{-10}	...	$>1100_{-220}$
S II	350^{+16}_{-16}	720^{+120}_{-140}	720^{+190}_{-200}
Fe II	$11\,000^{+950}_{-950}$	...	$>18\,000_{-2700}$
Ni II	880^{+66}_{-66}	900^{+230}_{-230}	900^{+290}_{-290}

measurements of the remaining levels in order to calculate the total Fe II column density.

3.2 Photoionization modelling

In order to determine N_H and U_H, we use the spectral synthesis code Cloudy (version c17.00, Ferland et al. 2017) to create photoionization models with a given hydrogen column density (N_H) and ionization parameter (U_H), following previous works (e.g. Xu et al. 2019; Miller et al. 2020a, b; Byun et al. 2022a, b). For these models, we assume solar metallicity and the spectral energy distribution (SED) of quasar HE0238-1904 (Arav et al. 2013, see their fig. 10). Together, these parameters determine the column density of each ion in a photoionization model. We can therefore create a grid of models over a range of N_H and U_H and compare them to our measured ionic column density. The model with the lowest χ^2 gives a solution that best matches our observations. The best-fitting solution for S5 gives us $\log N_H = 21.34^{+0.24}_{-0.33}$ cm^{-2} and $\log U_H = -1.75^{+0.28}_{-0.45}$. The 'Adopted' column of Table 2 lists the column densities used for this fit. Fig. 3 shows a visualization of this solution.

3.3 Electron number density

The ratios of excited state to ground state column densities can be used to determine the electron number density of an absorber (Moe et al. 2009). This can become difficult to measure directly if the ground or excited state troughs in a spectrum are significantly blended, or if the ground state trough is saturated. In this case, we can use the Synthetic Spectral Simulation method (SSS) in order

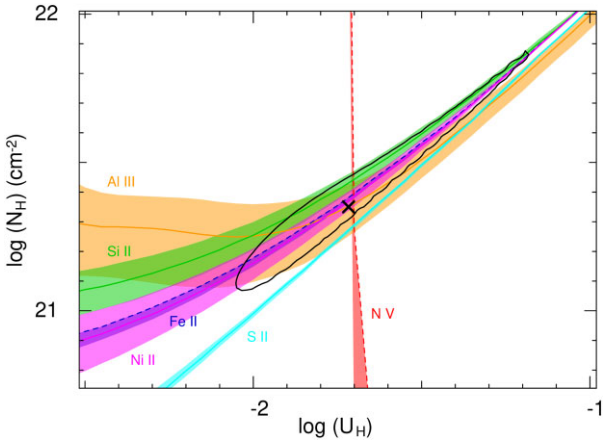

Figure 3. Photoionization solution for the main system of J1130. The coloured lines represent the allowed values of N_H and U_H for a given $N_{\rm ion}$. Solid lines represent measurements, and dashed lines represent lower limits. The coloured ribbons around these lines represent the errors of these measurements. The solution, found by χ^2 minimization, is displayed as a black cross, and the black contour represents the 1σ error for this solution. Only the ions that affected the solution are shown.

Table 3. Properties of the main system in J1130 + 0411.

log (N_H) ($\rm cm^{-2}$)	$21.44^{+0.24}_{-0.33}$
log (U_H) (dex)	$-1.75^{+0.28}_{-0.45}$
log(n_e) ($\rm cm^{-3}$)	$2.6^{+0.8}_{-0.7}$
R (kpc)	16^{+23}_{-11}
$\dot{M}$ ($\rm M_\odot\ yr^{-1}$)	4100^{+6600}_{-2400}
log ($\dot{E}_k$) (erg $\rm s^{-1}$)	$46.13^{+0.41}_{-0.37}$
$\dot{E}_k/L_{\rm Edd}$ (per cent)	$1.4^{+2.2}_{-0.8}$

to help determine $n_{\rm e}$ (Xu et al. 2020b). For this method, we input the previously obtained photoionization solution, with a range of $n_{\rm e}$, into Cloudy to get the total column densities of the desired ions. From the wavelength, oscillator strength, excited ionic critical densities, and output column density of each absorption line, we create synthetic, theoretical spectra with the range of $n_{\rm e}$. We then find the synthetic spectrum that best matches the observed spectrum in order to determine the best-fitting $n_{\rm e}$ for that absorption system. Since we use a fixed metallicity and SED, N_H affects the total strength of all lines, and U_H affects the relative strength between different ions. Excited ions are mostly populated by collisions between free electrons and ground state ions (Osterbrock & Ferland 2006), so $n_{\rm e}$ affects the relative strength between the ground state and various excited states of ions.

Table 3 gives a determination of $n_{\rm e}$ for S5 of J1130 + 0411 and Fig. 4 shows the SSS plots used to find this solution. Note that these fits have a high reduced χ^2 (also given in Fig. 4). Certain phenomena unrelated to fitting $n_{\rm e}$ contribute to this, such as the unidentified line at observed wavelength 7968 Å in the left plot of Fig. 4 and the atmospheric lines from 8932 to 8970 Å in the right plot. However, the largest contribution to this χ^2 comes from the fact that the best-fitting SSS method overpredicts the strength of the Fe II* 1873 $\rm cm^{-1}$ energy level transitions and underpredicts the strength of all other Fe II* energy level transitions, resulting in a poor fit overall. This discrepancy is discussed further in Section 5.2. In order to determine the positive and negative errors, we increase and decrease (respectively) the input $n_{\rm e}$ until the simulated spectrum has double the χ^2 compared with the best fit. From the SSS method, we determine $\log n_e = 2.6^{+0.8}_{-0.7}$ $\rm cm^{-3}$. We also note that increasing N_H by 0.1 dex slightly increases the quality of the fit, so we adopt for this system $\log N_H = 21.44^{+0.24}_{-0.33}$ $\rm cm^{-2}$.

4 DISTANCE AND ENERGETICS

We can determine the distance R from the outflow to the central source using the definition of the ionization parameter,

$$U_H \equiv \frac{Q_H}{4\pi R^2 n_H c}, \tag{6}$$

where Q_H is the incidence rate of hydrogen-ionizing photons, $n_{\rm H}$ is the number density of hydrogen, which for a highly ionized plasma is estimated as $n_{\rm e} \approx 1.2 n_{\rm H}$, and c is the speed of light (Osterbrock & Ferland 2006).

We can determine Q_H by taking the continuum flux at rest wavelength $\lambda = 1495$ Å from the SDSS data ($F_\lambda = 1.32^{+0.07}_{-0.07} \times 10^{-16}$ erg $\rm s^{-1}$ $\rm cm^{-2}$ $\rm Å^{-1}$) and scaling it to match the HE0238 SED. Integrating this spectrum over all energies above 1 Ryd gives $Q_H = 5.8^{+0.3}_{-0.3} \times 10^{57}$ $\rm s^{-1}$, and the corresponding bolometric luminosity is $L_{\rm bol} = 9.2^{+0.5}_{-0.5} \times 10^{47}$ erg $\rm s^{-1}$. For this system, we determine $R = 16^{+23}_{-11}$ kpc.

With the distance of the outflow, we can calculate the outflow mass (Borguet et al. 2012),

$$M \simeq 4\pi \Omega R^2 N_{\rm H} \mu m_p, \tag{7}$$

where Ω is the global covering factor (i.e. the fraction of the total solid angle 4π of the quasar that the outflow covers, ~0.2 for BALQSOs; Hewett & Foltz 2003; see section 5.2 of Dunn et al. 2010), $\mu = 1.4$ is the mean atomic mass per proton, and $m_{\rm p}$ is the proton mass. From there, we can divide by the dynamical time-scale to get the average mass flow rate,

$$\dot{M} \simeq 4\pi \Omega R N_{\rm H} \mu m_p v, \tag{8}$$

where v is the outflow velocity. The kinetic luminosity is then

$$\dot{E}_k \simeq \frac{1}{2}\dot{M} v^2. \tag{9}$$

For this system, we calculate $\dot{M} = 4100^{+6600}_{-2400}$ $\rm M_\odot\ yr^{-1}$ and $\log \dot{E}_k = 46.13^{+0.41}_{-0.37}$ erg $\rm s^{-1}$. Table 3 summarizes all calculated properties.

4.1 Error propagation

The thin, elliptical shape of the photoionization solution (see Fig. 3) demonstrates that the $N_{\rm H}$ and $U_{\rm H}$ errors are correlated with each other. In order to see how this could affect our error estimates, we calculate three values ζ^+, ζ, and ζ^- that correspond to the top-right corner, middle solution, and bottom-left corner of the photoionization

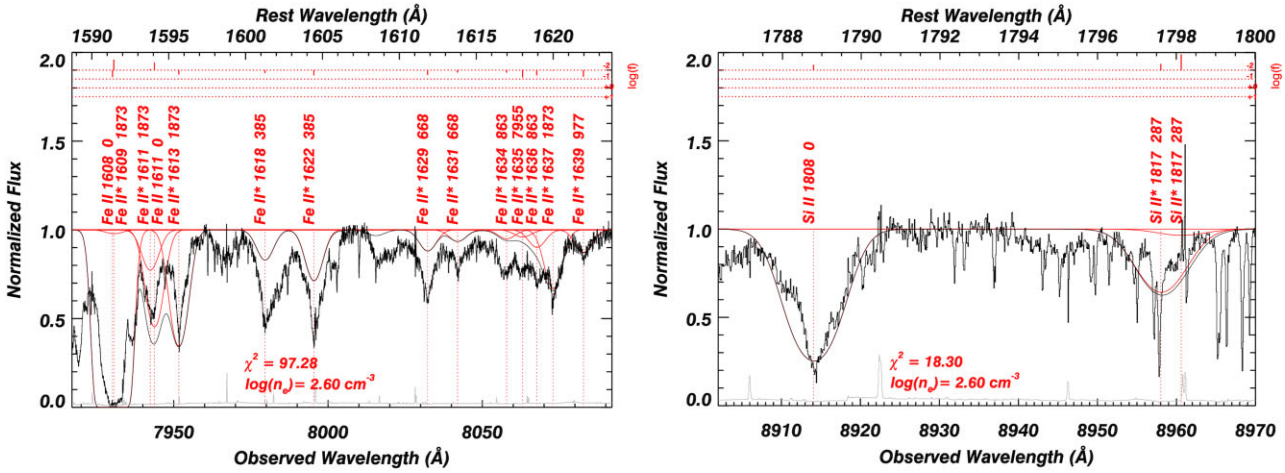

Figure 4. SSS plots of the Fe II/Fe II* and Si II/Si II* lines in the main system of J1130 + 0411 that we use to find n_e. The logarithm of the oscillator strength of each line is shown in red at the top with a separate y-axis. The n_e used to create the spectrum is shown at the bottom of the plot, along with the reduced χ^2.

solution contour, respectively, so that $\dot{M} = \zeta * \sqrt{Q_H/n_e}$:

$$\zeta^+ = \mu m_p 4\pi\Omega v * \left(N_H + \sigma^+_{N_H}\right) * \sqrt{1.2/4\pi c * \left(U_H + \sigma^+_{U_H}\right)},$$
$$\zeta = \mu m_p 4\pi\Omega v * N_H * \sqrt{1.2/4\pi c * U_H},$$
$$\zeta^- = \mu m_p 4\pi\Omega v * \left(N_H - \sigma^-_{N_H}\right) * \sqrt{1.2/4\pi c * \left(U_H - \sigma^-_{U_H}\right)}, \quad (10)$$

where $\sigma^+_{N_H}$, $\sigma^-_{N_H}$, $\sigma^+_{U_H}$, and $\sigma^-_{U_H}$ are the positive and negative errors for N_H and U_H given in Table 3. Now, we want to make sure that $\zeta^+ > \zeta$ and $\zeta^- < \zeta$. Since $\zeta \propto N_H/\sqrt{U_H}$, this requires satisfying the following condition:

$$\frac{N_H}{\sqrt{U_H}} < \frac{\left(N_H + \sigma^+_{N_H}\right)}{\sqrt{U_H + \sigma^+_{U_H}}}, \qquad \frac{N_H}{\sqrt{U_H}} > \frac{\left(N_H - \sigma^-_{N_H}\right)}{\sqrt{U_H - \sigma^-_{U_H}}}.$$

If these inequalities do not hold, then we simply swap the definitions of ζ^+ and ζ^-. Finally, we define $\sigma^+_\zeta = \zeta^+ - \zeta$ and $\sigma^-_\zeta = \zeta - \zeta^-$ and add to this in quadrature the errors of n_e and Q_H:

$$\log \sigma_{\dot{M}} = \sqrt{\left(\log \sigma_\zeta\right)^2 + \frac{1}{4}\left[\left(\log \sigma_{n_e}\right)^2 + \left(\log \sigma_{Q_H}\right)^2\right]}, \quad (11)$$

where the factor of 1/4 comes from the fact that R is proportional to the square root of n_e and Q_H. In the end, for S5, this method produces errors that are a factor of ∼1.3 lower than those calculated by simply adding the R and N_H errors in quadrature.

5 DISCUSSION

5.1 Contribution to AGN feedback

In order to numerically compare our calculated $\dot{E}_k$ with L_{Edd}, we must first determine L_{Edd} for J1130 + 0411. To do this, we take advantage of a method introduced by Coatman et al. (2016), in which they use the width of the C IV emission line to determine the mass of the black hole (see their equations 4 and 6). This method is based on that used by Vestergaard & Peterson (2006). Modelling the C IV emission in this object is difficult as it is heavily blended with absorption. However, it is the only emission feature visible in the spectrum of J1130 + 0411 that we can use to determine the black-hole mass. So, to approach this, we centre a Gaussian on the C IV λ1549 Å emission line and fit it to an unblended portion of the red wing in order to get the full-width at half maximum. Fig. 5 shows this Gaussian fit. From there, it is simple to calculate L_{Edd} (Osterbrock & Ferland 2006), and we derive for this system $L_{Edd} = 9.7^{+1.7}_{-1.4} \times 10^{47}$ erg s^{-1}. Our calculated $\dot{E}_k$ for S5 is then $1.4^{+2.2}_{-0.8}$ per cent of the L_{Edd} of J1130 + 0411. This is above the 0.5 per cent threshold suggested by Hopkins & Elvis (2009), thus we conclude that the main system has the potential to contribute to AGN feedback.

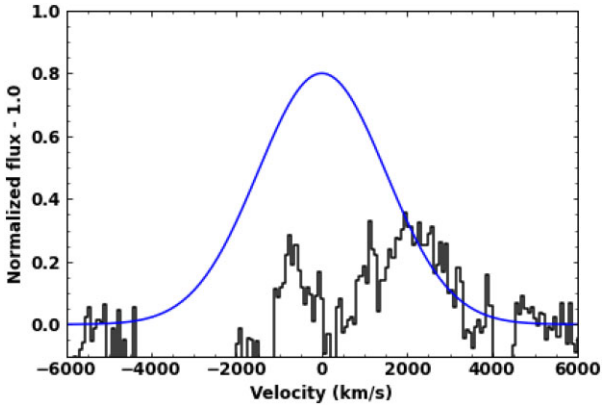

Figure 5. Gaussian fit to the C IV emission. Normalized flux – 1 as a function of velocity is displayed in black. The Gaussian curve is displayed in blue and is centred on $v = 0$ km s^{-1}. Note that there is heavy absorption in the vicinity of C IV λ1549. We fit the Gaussian by eye to the relatively unblended right wing of the C IV emission.

5.2 Comparison with other outflows

Other observations of outflows containing Fe II* absorption have been performed. In SDSS J1439-0106, Byun et al. (2022a) compare the abundance ratios of five different Fe II* energy levels to the ground state and find that the 1873 cm^{-1} level is in agreement with the other four. Xu et al. (2021) measure multiple excited Fe II energy levels up to 21 580 cm^{-1} in Q0059-2735, however, no 1873 cm^{-1} troughs were reported. Choi et al. (2020) also report multiple excited states with the exclusion of 1873 cm^{-1} in SDSS J1352 + 4239. Several excited levels are measured in QSO 2359-1241 by Korista et al. (2008), including three 1873 cm^{-1} lines: 2332, 2349, and 2361 Å. However, as they note, these troughs are blended with other lines.

All of these lines are out of range of the J1130 + 0411 data. It appears that the Fe II 2332, 2349, 2361, and 2494 Å lines detected in FBQS 0840 + 3633 by de Kool et al. (2002) are of the 1873 cm^{-1} excited level, but these are also heavily blended and out of the spectral range of J1130 + 0411.

Blending of Fe II* 1873 cm^{-1} with other Fe II lines is also a problem in J1130 + 0411. Although this is somewhat mitigated by using the SSS method, this method is not perfect and assumes an AOD scenario for every trough. The spectral synthesis procedure *SimBAL* (Leighly et al. 2018) provides a similar approach to SSS, but instead implements a power-law method (Arav et al. 2005; Leighly et al. 2019) in order to create synthetic spectra. Future studies could use *SimBAL* to attempt to model the Fe II lines in J1130 + 0411 in that way.

We also note that the average mass flow rate of $\dot{M} = 4100^{+6600}_{-2400}$ $M_\odot$ yr^{-1} is particularly large. Byun et al. (2022b) find an even higher-mass flow rate of 6500^{+8900}_{-3400} $M_\odot$ yr^{-1} in their S2 of quasar SDSS J0242 + 0049. These rates are roughly 10 times greater than the highest of which reported by Choi et al. (2022), with the largest in their sample, J1154 + 0300, having only $\dot{M} \sim 500$ $M_\odot$ yr^{-1}. Comparing J1130 + 0411 with relatively similar objects in this sample, we conclude that our larger $\dot{M}$ can be attributed to both a higher outflow velocity and outflow distance in S5. Our $L_{bol} = 9.2^{+0.5}_{-0.5} \times 10^{47}$ erg s^{-1} is higher than the largest bolometric luminosity in the Choi et al. (2022) sample by ∼0.5 dex, and our $\log \dot{E}_k = 46.13^{+0.41}_{-0.37}$ is comparable to the the highest values in their sample. Additionally, the systemic redshift $z = 3.98$ of J1130 + 0411 is significantly higher than the lower redshift quasars, with $0.66 < z < 1.63$, targeted by Choi et al. (2022).

5.3 Other absorption systems in J1130 + 0411

We identify seven absorption systems in this quasar other than the main system. We order these in terms of decreasing velocity, so that S1 (−15 400 km s^{-1}) is the highest velocity system and S8 (−2400 km s^{-1}) is the lowest velocity system. S1 was identified by Chen et al. (2021; see Section 2.1). The presence of wide, smooth C IV troughs and the unblended red Si IV trough lead us to believe that this system is an outflow. S2 has C IV and Si IV troughs, but as they are very narrow, this is most likely an intervening system. Although we observe C II* in S3, the fact that we do not observe any Si IV is again indicative of an intervening system. Many of the expected lines in S4 fall in the blue end of the S5 BALs, leading us to believe that this system is actually subcomponent of S5. S5 is the main system discussed in the bulk of this paper. In S6, we see some excited state ions, though blended, and many of the ions we expect to see in quasar outflows, so this system is most likely an outflow. S7 and S8 also show (blended) C II* troughs, so these are most likely outflows as well.

Unfortunately, all of these systems aside from S5 have few unblended diagnostic troughs from which to extract reliable ionic column densities. In addition, no unblended excited troughs are identified in any of these weaker systems. Therefore, while we are able to get some information about N_H and U_H for some systems, we are not able to extract any electron number densities, and so we are not able to calculate any distances or energetics for these systems. Table 1 summarizes the properties of these systems that we were able to measure. Since S2 and S3 are intervening and thus their redshifts are likely cosmological, these redshifts are reported rather than their velocities in the footnotes of this table.

6 SUMMARY

We have presented the analysis of eight absorption systems, which we label S1-8, in quasar SDSS J1130 + 0411, with a focus on S5 in particular. The data for this object was taken by VLT/UVES and was pulled from the first SQUAD data release (Murphy et al. 2018). We determine a new systemic redshift $z = 3.98$ that differs both from the one reported by Chen et al. (2021) and that by the SDSS catalog. By measuring the column densities of the nine ions given in Table 2, we found a photoionization solution for N_H and U_H. We also determined information about N_H and U_H for some of the other systems using photoionization analysis.

By comparing the trough depth of excited and ground states of Fe II and Si II, we used the SSS method (Xu et al. 2020b) so as to determine a best-fitting n_e. However, this best-fitting synthetic spectrum was a rather poor fit, as it overpredicts the Fe II* 1873 cm^{-1} troughs while underpredicting all other observed Fe II* troughs. Additional observations of Fe II* excited states, including the 1873 cm^{-1} excited state, will show whether this is a recurring phenomenon in quasar spectra.

With measurements of N_H, U_H, and n_e, we determine an outflow distance $R = 16^{+23}_{-11}$ kpc and a kinetic luminosity to Eddington luminosity ratio $\dot{E}_k/L_{Edd} = 1.4^{+2.2}_{-0.8}$ per cent. Since models suggest that $\dot{E}_k$ must be at least 0.5 per cent − 5 per cent of L_{Edd} (Hopkins & Elvis 2009; Scannapieco & Oh 2004, respectively), we conclude that this system is capable of contributing to AGN feedback.

ACKNOWLEDGEMENTS

NA, AW, and DB acknowledge support from NSF grant AST 2106249, as well as NASA STScI grants AR-15786, AR-16600, and AR-16601. We also thank the anonymous referee whose constructive comments and suggestions helped to clarify and improve this paper.

DATA AVAILABILITY

The reduced and normalized VLT/UVES data for J1130 + 0411 is a part of the first SQUAD data release presented in Murphy et al. (2018). The SDSS data used to determine the systemic redshift, the width of the C IV emission, and the width of the C IV BAL is available on the SDSS archive.

REFERENCES

Anglés-Alcázar D., Davé R., Faucher-Giguère C.-A., Özel F., Hopkins P. F., 2016, MNRAS, 464, 2840
Arav N., Korista K. T., de Kool M., Junkkarinen V. T., Begelman M. C., 1999a, ApJ, 516, 27
Arav N., Becker R. H., Laurent-Muehleisen S. A., Gregg M. D., White R. L., Brotherton M. S., de Kool M., 1999b, ApJ, 524, 566
Arav N., Kaastra J., Kriss G. A., Korista K. T., Gabel J., Proga D., 2005, ApJ, 620, 665
Arav N., Borguet B., Chamberlain C., Edmonds D., Danforth C., 2013, MNRAS, 436, 3286
Arav N., Liu G., Xu X., Stidham J., Benn C., Chamberlain C., 2018, ApJ, 857, 60
Arav N., Xu X., Miller T., Kriss G. A., Plesha R., 2020, ApJS, 247, 37
Barlow T. A., Hamann F., Sargent W. L. W., 1997, in Aravm N., Shlosman I., Weymann R. J., eds, ASP Conf. Ser. Vol. 128, Mass Ejection from Active Galactic Nuclei. Astron. Soc. Pac., San Francisco, p. 13
Bennett C. L., Larson D., Weiland J. L., Hinshaw G., 2014, ApJ, 794, 135
Borguet B. C. J., Edmonds D., Arav N., Dunn J., Kriss G. A., 2012, ApJ, 751, 107
Byun D., Arav N., Walker A., 2022a, MNRAS, 516, 100

Byun D., Arav N., Hall P. B., 2022b, ApJ, 927, 176
Chamberlain C., Arav N., Benn C., 2015, MNRAS, 450, 1085
Chen C., Hamann F., Ma B., Murphy M., 2021, ApJ, 907, 84
Choi H., Leighly K. M., Terndrup D. M., Gallagher S. C., Richards G. T., 2020, ApJ, 891, 53
Choi H., Leighly K. M., Terndrup D. M., Dabbieri C., Gallagher S. C., Richards G. T., 2022, preprint (arXiv:2203.11964)
Ciotti L., Ostriker J. P., Proga D., 2009, ApJ, 699, 89
Coatman L., Hewett P. C., Banerji M., Richards G. T., Hennawi J. F., Prochaska J. X., 2016, MNRAS, 465, 2120
Dai X., Shankar F., Sivakoff G. R., 2008, ApJ, 672, 108
de Kool M., Arav N., Becker R. H., Gregg M. D., White R. L., Laurent-Muehleisen S. A., Price T., Korista K. T., 2001, ApJ, 548, 609
de Kool M., Becker R. H., Gregg M. D., White R. L., Arav N., 2002, ApJ, 567, 58
Dunn J. P. et al., 2010, ApJ, 709, 611
Edmonds D. et al., 2011, ApJ, 739, 7
Ferland G. J. et al., 2017, Revista Mexicana de Astronomía y Astrofísica, 53, 385
Gabel J. R. et al., 2005, ApJ, 631, 741
Hamann F., Sabra B., 2003, in Richards G. T., Hall P. B., eds, ASP Conf. Ser. Vol. 311, AGN Physics with the Sloan Digital Sky Survey. Astron. Soc. Pac., San Francisco, p. 203
Hamann F. W., Barlow T. A., Chaffee F. C., Foltz C. B., Weymann R. J., 2001, ApJ, 550, 142
Hewett P. C., Foltz C. B., 2003, AJ, 125, 1784
Hidalgo P. R., Hamann F., Eracleous M., Capellupo D., Charlton J., Shields J., 2012, in Chartas G., Hamann F., Leighly K. M., eds, ASP Conf. Ser. Vol. 460, AGN Winds in Charleston. Astron. Soc. Pac., San Francisco, p. 93
Hopkins P. F., Elvis M., 2009, MNRAS, 401, 7
Knigge C., Scaringi S., Goad M. R., Cottis C. E., 2008, MNRAS, 386, 1426
Korista K. T., Bautista M. A., Arav N., Moe M., Costantini E., Benn C., 2008, ApJ, 688, 108
Leighly K. M., Terndrup D. M., Gallagher S. C., Richards G. T., Dietrich M., 2018, ApJ, 866, 7
Leighly K. M., Terndrup D. M., Lucy A. B., Choi H., Gallagher S. C., Richards G. T., Dietrich M., Raney C., 2019, ApJ, 879, 27
Matteo T. D., Springel V., Hernquist L., 2005, Nature, 433, 604
McCarthy I. G. et al., 2010, MNRAS, 406, 822
Miller T. R., Arav N., Xu X., Kriss G. A., Plesha R. J., Benn C., Liu G., 2018, ApJ, 865, 90
Miller T. R., Arav N., Xu X., Kriss G. A., Plesha R. J., 2020a, ApJS, 247, 39
Miller T. R., Arav N., Xu X., Kriss G. A., Plesha R. J., 2020b, ApJS, 249, 15
Moe M., Arav N., Bautista M. A., Korista K. T., 2009, ApJ, 706, 525
Moll R. et al., 2006, A&A, 463, 513
Murphy M. T., Kacprzak G. G., Savorgnan G. A. D., Carswell R. F., 2018, MNRAS, 482, 3458
Murray N., Chiang J., Grossman S. A., Voit G. M., 1995, ApJ, 451, 498
Osterbrock D. E., Ferland G. J., 2006, Astrophysics of Gaseous Nebulae and Active Galactic Nuclei, 2nd edn. University Science Books, Sausalito, CA
Proga D., Stone J. M., Kallman T. R., 2000, ApJ, 543, 686
Savage B., Sembach K., 1991, ApJ, 379, 245
Scannapieco E., Oh S. P., 2004, ApJ, 608, 62
Stone R. B., Richards G. T., 2019, MNRAS, 488, 5916
Vayner A. et al., 2021, ApJ, 919, 122
Vestergaard M., Peterson B. M., 2006, ApJ, 641, 689
Xu X., Arav N., Miller T., Benn C., 2018, ApJ, 858, 39
Xu X., Arav N., Miller T., Benn C., 2019, ApJ, 876, 105
Xu X., Arav N., Miller T., Kriss G. A., Plesha R., 2020a, ApJS, 247, 42
Xu X., Arav N., Miller T., Kriss G. A., Plesha R., 2020b, ApJ, 247, 38
Xu X., Arav N., Miller T., Korista K. T., Benn C., 2021, MNRAS, 506, 2725

This paper has been typeset from a TEX/LATEX file prepared by the author.